

# MIST-net: Multi-domain Integrative Swin Transformer network for Sparse-View CT Reconstruction

Jiayi Pan<sup>1</sup>, Weiwen Wu<sup>1</sup>, Zhifan Gao<sup>1</sup> and Heye Zhang<sup>1</sup>

<sup>1</sup>School of Biomedical Engineering, Sun Yat-sen University, Shenzhen

**Abstract:** The deep learning-based tomographic image reconstruction methods have been attracting much attention among these years. The sparse-view data reconstruction is one of typical underdetermined inverse problems, how to reconstruct high-quality CT images from dozens of projections is still a challenge in practice. To address this challenge, in this article we proposed a Multi-domain Integrative Swin Transformer network (MIST-net). First, the proposed MIST-net incorporated lavish domain features from data, residual-data, image, and residual-image using flexible network architectures. Here, the residual-data and residual-image domains network components can be considered as the data consistency module to eliminate interpolation errors in both residual data and image domains, and then further retain image details. Second, to detect the image features and further protect image edge, the trainable Sobel Filter was incorporated into the network to improve the encode-decode ability. Third, with the classical Swin Transformer, we further designed the high-quality reconstruction transformer (i.e., Recformer) to improve the reconstruction performance. The Recformer inherited the power of Swin transformer to capture the global and local features of the reconstructed image. The experiments on the numerical datasets with 48 views demonstrated our proposed MIST-net provided higher reconstructed image quality with small feature recovery and edge protection than other competitors including the advanced unrolled networks. The quantitative results show that our MIST-net also obtained the best performance. The trained network was transferred to the real cardiac CT dataset with 48 views, the reconstruction results further validated the advantages of our MIST-net, which demonstrated the good robustness of our MIST in clinical applications.

## I . Introduction

Computed Tomography (CT) Imaging has been widely used in the field of medical diagnosis and industrial detection because of its excellent imaging ability [1]. Especially in 2020, CT became an essential technology to detect and diagnose the COVID-19 [2]. Although CT scans provide practical and accurate diagnostic results, they are also increasingly harmful to the human body due to radiation [3]. High radiation may result in the high risk of disease. An effective approach to reduce radiation dose is sparse-view CT reconstruction [4, 5], which means only one part of projection data can be used for the image reconstruction. In this case, the traditional reconstruction algorithms such as filtered back-projection (FBP) [6] may contribute to serious streaking artifacts. These artifacts can result in too low image quality to diagnose and treatment.

Since the emergence of artificial intelligence [7-10], many deep learning-based methods have been developed to improve the quality of sparse-view CT reconstruction [11-13]. They

can be divided into three categories: image domain restoration [14], dual-domain restoration [15] [16], and iterative reconstruction methods [17] [18]. For the image domain restoration methods, they are also called post-processing methods. They can directly process low quality images as the input and ground truth as outputs, which means that this kind of methods don't need raw projections data. The classical reconstruction networks includes FBPconvNet [14], Densenet Deconvolution Network (DD-Net) [12] and residual encoder-decoder CNN (RED-CNN) [11]. Zhang et al. [19] used a generative adversarial network (GAN) to remove sparse views artifacts. Wang et al. [20] presented a limited-angle CT image reconstruction algorithm based on a U-net convolutional neural network, which can effectively eliminate the noise and the artifacts while preserving the image structures. The image post-processing methods always enjoy a simple structure and easy to be implemented. Since there is no projection data playing the game, it is difficult to remove severe streak artifacts and accurately recover image details and features.

The dual-domain based deep reconstruction methods usually concentrated to reconstruct high-quality image by complementing the missing data in both projection domain and image domain. For examples, Hu et al. [21] proposed a Hybrid Domain neural Network (HDNet), which recovered projection and image information successively and perform better than single domain methods. Liu et al. [22] presented a lightweight structure aimed to utilize spatial correlation for sparse-view CT reconstruction. Zhang et al. [23] designed a hybrid-domain convolutional neural network for limited-angle computed tomography imaging. Wu et al. [24] presented a Dual-domain Residual-based Optimization NEtwork (DRONE), which performed well in edge preservation and details recovery. The dual-domain network can also be applied to 3D reconstruction [25]. However, the final images may suffer from secondary artifacts due to the errors introduced in the process of projections domain interpolation.

Inspired by the classic iteration reconstruction algorithm, deep reconstruction networks can also be designed by unfolding an iterative mechanism. Cheng et al. [26] accelerated iterative reconstruction with the help of deep learning. Chen et al. [27] presented a Learned Experts' Assessment-based Reconstruction Network (LEARN) for sparse-view data reconstruction. Zhang et al. [28] extended the LEARN model to a dual-domain version, named LEARN++. Xiang et al. [29] proposed a Fast Iterative Shrinkage Thresholding Algorithm (FISTA) for inverse imaging problems. In [30], a deep learning enabled prior image constrained compressed sensing (DL-PICCS) reconstruction framework was proposed for sparse-view reconstruction. Iterative reconstruction algorithms contribute to suppress noise and improve image quality. Nevertheless, iterative reconstruction methods need huge GPU memory and lead in this kind of reconstruction method is difficult to be extended with 3D geometry.

In this work, we proposed a Multi-domain Integrative Swin Transformer network (MIST-net) to reconstruct high quality CT images from sparse-view projections. The overall of network architecture consists of three key components: initial recovery, data consistency correction and high-fidelity reconstruction. In the initial recovery, a data-extension encoder-decoder block is first employed to extend sparse-view projection data to full-view projection data by interpolation operation. Then, an end-to-end model named as the edge enhancement reconstruction network reconstructed the initial image to remove sparse artifacts and protect image edges. However, projections domain interpolation may introduce errors and further result in unexpected artifacts. Therefore, the data consistency module, where two residual

sub-networks (one for residual projection estimation, the other one for residual image correction) was introduced to reduce errors and improve structural details. Although the CNN-based deep learning reconstruction methods often have a good effect, it cannot learn global and long-range image information interaction well due to the locality of convolution operation. Fortunately, transformers [31] have such ability in long-range modeling and show good performance in nature language processing (NLP) tasks [32-34]. The propose of Vision Transformer [35] shows that transformer can take the place of convolutions in some image processing tasks [36-38]. Therefore, we introduce a Hierarchical Vision Transformer using Shifted Windows [38] in the high fidelity reconstruction module to remedy the shortcoming of convolution. It captures the long-range dependencies and help to reconstruct better images.

Compared with the CNN-based deep networks developed for the sparse-view reconstruction in the past few years, our MIST-net is innovative in several aspects. First, an encode-decode [39] structure is employed in the initial recovery module to extract deep features in the data and image domain simultaneously. Especially, an edge enhancement reconstruction network in the image domain to recover good images with boundaries enhancement was designed. Second, the data-residual and image-residual networks are used in the data consistency module to eliminate errors in both projections and images domain, which contributes to artifacts reduction and subtle structure recovery. Third, the Swin reconstruction transformer (Recformer) extracts both shallow and deep features in the image domains to ensure final reconstruction results of our MIST-net.

The organization of the paper is as follows. In the section II, we first introduce the basic theory and then describe our proposed MIST-net carefully. In section III, the reconstruction experiments result from our MIST and competitors are reported, showing the advantages of MIST-net. In section IV, we further implement the detailed ablation study including numerical and real cardiac data. We also do noise analysis experiments to verify the robustness of the model. In the last section, we discuss our results as well as make conclusions of this work.

## II. Method

### A. CT Imaging Model

The ideal mathematical model of CT imaging can be expressed as a discrete linear system:

$$y = Ax + b \quad (1)$$

where  $x$  represents a reconstructed CT image, and it can be expressed as  $x = [x_1, x_2, x_3, \dots, x_p]$ .  $y$  stands for the measured projection data, and it can be written as  $y = [y_1, y_2, y_3, \dots, y_Q]$ .  $b$  stands for projection noise, and  $A$  is a CT system matrix, which contains  $P \times Q$  elements. Due to the noise in  $y$ , the solution of Eq. (1) can be obtained by minimizing the following objective function:

$$\min_x \|Ax - y\|_F^2 \quad (2)$$

where  $\|\cdot\|_F^2$  stands for the Frobenius norm. The ART or SART are usually employed to minimize the Eq. (2) [40]. However, solving  $x$  directly from a very sparse projection data  $y$  is an under determined inverse problem, which may lead to the poor reconstructed image quality with streak artifacts. To address this problem, a regularization term representing prior knowledge is usually introduced to obtain better reconstruction result, then we have

$$\min_x \left( \|Ax - y\|_F^2 + \beta_h h(x) \right) \quad (3)$$

There are two components in Eq. (3), i.e. the fidelity term  $\|Ax - y\|_F^2$  and the regulation prior knowledge term  $h(x)$ . The hyperparameter  $\beta_h$  is designed to balance these two components. By the way, different reconstruction methods correspond different regularization priors such as total variation [41, 42] and dictionary learning [43-45].

### **B. Multi-domain Integrative Network**

In projections domain, the main work is to complement and restore the sparse-view sinograms. For example, Dong et al. [46] completed the missing data with U-Net architecture, then an typical network is further refine the raw image reconstructed from completed projections. The benefit of projection domain deep neural network is that it can reduce the data error from the view of detector measurement. However, the interpolated projection with deep neural network may introduce wrong measurement and further result in false positive and false negative diagnosis results. Unfortunately, the false results are also difficult to be correct even if by a high-fidelity post-processing image domain network. To overcome this challenge, the residual-data domain sub-network is first considered to correct the data inconsistency of the initial reconstructed image. Indeed, the stage is benefit to correct original data error to overcome the data inconsistency. Furthermore, one residual-image domain sub-network further improves the reconstruction performance. Finally, Swin transformer architecture can deep characterize various latent features of the reconstructed image to capture local and global information of image-self.

### **C. Edge Detection Operator**

The edge of images was one of the most important features, including a wealth of internal information especially in medical images, for example, the edge of tumor helps to diagnose if it is benign or malignant. In this work, we introduced a Sobel filter [47] to overcome the problem of excessive edge smoothing. Sobel operator belonged to orthogonal gradient operator and its gradient corresponded to first derivative. For a continuous function  $g(a,b)$ , where  $(a, b)$  indicates the position point, the gradient can further be expressed as a vector:

$$\nabla g(a, b) = \{G_a, G_b\} = \left\{ \frac{\partial g}{\partial a}, \frac{\partial g}{\partial b} \right\} = \frac{\partial g}{\partial a} i + \frac{\partial g}{\partial b} j \quad (4)$$

$$\text{mag}(\nabla g) = |\nabla g| = \sqrt{\left(\frac{\partial g}{\partial a}\right)^2 + \left(\frac{\partial g}{\partial b}\right)^2} \quad (5)$$

$$\theta(a, b) = \arctan\left(\frac{G_a}{G_b}\right) \quad (6)$$

where the  $\text{mag}(\nabla g)$  and  $\theta(a, b)$  stand for the magnitude and direction angle of  $\nabla g(a, b)$ . The

partial derivatives needed to be calculated for each pixel point by using the equation (6). Original Sobel operator contains a  $3 \times 3$  vertical filter and a  $3 \times 3$  horizontal filter, which has a maximum response to the vertical edge and the level edge respectively.

Liang et al. [48] proposed an edge enhancement-based densely connected network (EDCNN) and achieved good performance in low-dose CT denoising. Sharifrazi et al. [49] applied Sobel filter to achieve accurate detection of COVID-19 patients from CT images. Compared to other edge operator, the mechanism of Sobel is the differential of two rows or two columns, it can fully enhance elements on both sides, which made the edge seems more obvious. In this work, in addition to the level and vertical filter, we further add diagonal filter to our network in [48].

#### **D. Vision Transformers**

The original Transformer was first proposed for natural language processing (NLP). Transformer was similar to an encoder-decoder structure which consists with multi-head self-attention blocks, normalization layers and point-wise feed-forward networks. The Vision Transformer (ViT), proposed by Dosovitskiy et al. [35], which can be considered as the first vision transformer backbone for image classification. ViT had demonstrated the effectiveness of Transformer in CV tasks, although it required huge parameter and memory because the global computation led to quadratic complexity. To reduce the usage of GPU memory and number of calculation parameters, Swin Transformer [38] computed self-attention within local windows. The computational complexity of a global MSA module and a window based on an image patches with the size of  $n \times n$  are respectively recorded as  $\Omega(4n^2C^2 + 2n^4C)$  and  $\Omega(4n^2C^2 + 2M^2n^2)$ , where  $n^2$ ,  $C$  and  $M$  are image patch number, channel number of the hidden layers and window size. To solve the global modeling problem caused by local windows, Swin transformer designed a shifted window to strengthen the connection between adjacent windows. Due to its impressive performance, transformer has also been introduced to medical image processing. Chen et al. [50] proposed TransUNet, which claimed to be the first transformer based medical image segmentation Network. Recently, Eformer [51] used the self-attention and depth-wise convolution for better local context capture in medical image denoising. Our novel network MIST-net was developed to explore transformer in sparse-view data reconstruction. Again, we designed a Swin Recformer sub-network by combining Swin transformer and convolution layer to make full use of both shallow and deep features.

#### **E. MIST-net**

Figure 1 illustrated the flowchart of our proposed MIST-net. There are three key components, i.e., initial recovery, data consistency and high-definition reconstruction. Both initial recovery and data consistency have two sub-networks, one works in radon domain and the other was designed within images domain.

**1) Initial Recovery Module:** The architecture of this module is shown in Fig. 1. The first block of this module is an encoder-decoder block with a linear interpolation at the beginning. This part is designed to restore a sparse-view projection data  $z_0$  to a full-view projection data  $z_1$ . This is achieved by a projection domain sub-network  $z_1 = \Phi_1(z_0)$ . At the first layer of initial reconstruction is the network-based image reconstruction, i.e., FBP layer. An edge

enhancement reconstruction sub-network was employed to process the FBP layer output and further obtain a clearer and faithful image  $s_1$ . The initial recovery module can be expressed as follows:

$$s_1 = \Phi_2(\Phi_1(z_0)) \quad (7)$$

where  $\Phi_2$  represents the reconstruction sub-network from the initial recovery module.

**2) Data Consistency Module:** The errors are always introduced in projections and images because of the interpolation in Radon domain cannot accurately predict the missing original data. In addition, the following reconstruction sub-network in images domain may result in false positive and negative results. These errors may cause the secondary artifacts to compromise the quality of images. Data consistency module consists of two parts: the projection-residual processing sub-network  $\Phi_3$  and the image-residual processing sub-network  $\Phi_4$ . Here, we use two encoder-decoder blocks to handle residual data. The re-sampled residual data from  $s_1$  can be expressed as  $z_1 - z_2$ , where  $z_2$  represents the projection data from the image  $s_1$ . The estimated projection data residual  $z_3$  of the data consistency module is expressed as:

$$z_3 = \Phi_3(z_1 - z_2) \quad (8)$$

In addition to the data difference computed by the trained data residual network according to Eq. (5), there is also an image difference between the output of the initial recovery module and desired image. Here, the image residual processing sub-network was further employed to reduce the data inconsistency. The output of the image residual processing sub-network  $\Phi_4$  is as follows:

$$s_2 = \Phi_4(z_3) \quad (9)$$

Then, we can get the middle reconstruction output by adding the output of initial recovery module to the results of data consistency module, we have that

$$s_3 = s_1 + s_2 \quad (10)$$

**3) High-definition Reconstruction Module:** The sparse-view projection may lead to serious streaking artifacts in CT images especially when the number of views is extremely scanty. The function of this module is similar to post-processing methods which learn mappings from poor images to clear images. In traditional image super-resolution and denoising tasks, SwinIR [52] has achieved great success by using Swin transformer as a backbone. In this part, we propose a hybrid architecture called Swin Recformer, which is based on both convolution layers and Swin transformer layers to implement the image reconstruction task. As shown in Fig. 1 (d), the Swin Recformer contains convolution layers, Swin transformer mixed convolution (STC) units and a few residual connections. Each STC unit consists of six transformer layers as well as one convolution layer.

In this section, we will provide architecture details of the STC unit. A STC unit contains six Swin transformer layers and a  $3 \times 3$  convolution layer. Swin transformer block contains 2 core

designs which are described below. First, Swin transformer first designed a non-overlapping window-based multi-head self-attention (W-MSA) block, which can learn the long-range information correlation in a small-size window region (for example, a 16×16 feature map). Second, the shifted window-based multi-head self-attention (SW-MSA) block, which adds shifted windows to improve interactions between different windows. In the lower right of the Fig. 1 (d), two successive Swin transformer blocks are presented. Each Swin transformer block is successively composed of LN layer, multi-head self-attention (MSA) mechanism, residual connection and MLP. The window based multi-head self-attention (W-MSA) mechanism and the shifted window-based multi-head self-attention (SW-MSA) mechanism make up two adjacent transformer blocks. With the shifted window partitioning design, consecutive Swin transformer blocks are computed as:

$$\hat{x}^l = W - MSA(LN(x^{l-1})) + x^{l-1} \quad (11)$$

$$x^l = MLP(LN(\hat{x}^l)) + x^l \quad (12)$$

$$\hat{x}^{l+1} = SW - MSA(LN(x^l)) + x^l \quad (13)$$

$$x^{l+1} = MLP(LN(\hat{x}^{l+1})) + \hat{x}^{l+1} \quad (14)$$

where  $\hat{x}^l$  and  $x^l$  denote the output features of the W-MSA/SW-MSA module and the MLP module for block l, respectively; W-MSA and SW-MSA denote window based multi-head self-attention using regular and shifted window partitioning configurations, respectively. Same as the traditional transformer methods, self-attention is computed as follows:

$$\text{Attention}(Q, K, V) = \text{SoftMax}\left(\frac{QK^T}{\sqrt{d}} + B\right) \cdot V \quad (15)$$

where  $Q, K, V \in R^{M^2 \times d}$  are the query, key and value matrices; d is the query/key dimension, and  $M^2$  is the number of patches in a window. Since the relative position along each axis lies in the range  $[-M+1, M-1]$ , we parameterize a smaller-sized bias matrix  $\hat{B} \in R^{(2M-1) \times (2M+1)}$ , and values in B are taken from  $\hat{B}$ . After six Swin transformer blocks, a 3×3 convolution layer was added to enhance feature. Between adjacent STC units, a residual connection was used to aggregate feature maps generated from transformer and convolution.



### III. Experiments Results

Our model was designed and trained in Python using the PyTorch framework. All experiments were run on a PC with 48G NVIDIA RTX A6000 GPU, Intel(R) Xeon(R) Gold 6242R CPU @ 3.10GHz and 128GB RAM. The configuration of the training network is as follows. Our network was trained by Adam optimizer and the learning rate was set to 0.00025. The number of epochs was 50 and batch size is 1. FBPconvNet [14], HDNet [21], DDNet [12] and FISTA [29], are treated as comparisons. The root mean square error (RMSE), peak signal-to-noise ratio (PSNR) and structure similarity index (SSIM) are introduced to quantitatively assess the reconstruction results.

#### A. Simulated Data Result

To validate the feasibility of proposed network, we train and test our model on 2016 NIH-AAPM-Mayo Low-dose CT Grand Challenge datasets [53]. The datasets were derived from Siemens Somatom Definition CT scanners at 120kVp and 200mAs. To generalize our model to the real datasets which related in next section, we rearranged the datasets and keep all scanning parameters and configuration be consistent with the following real datasets. Specifically, the distances from x-ray source to the system isocenter and detector are set to 53.85cm and 103.68cm. The number of detector units and views are set to 880 and 2200 respectively. The size of reconstructed CT images is 512×512. Finally, a total number of 4,665 sinograms of 2,200×880 pixels were acquired from 10 patients at the normal dose setting, where 4,274 sinograms of 8 patients were employed for network training, and the rest 391 sinograms from the other 2 patients for network testing.

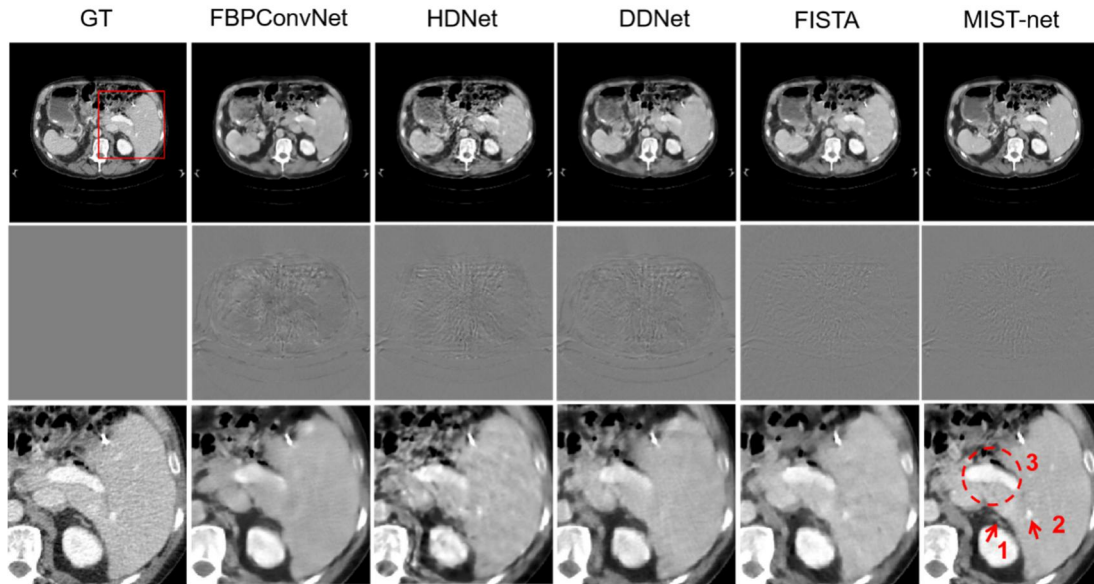


Fig. 2. Visualizations of sparse-view reconstruction in case 1 by using different methods. The 1<sup>st</sup>-6<sup>th</sup> columns represent ground truth (GT), FBPCConvNet, HDNet, DDNet, FISTA and MIST-net counterparts from 48 views. The 2<sup>nd</sup> row shows the difference images relative to the GT and 3<sup>rd</sup> represents the extracted region-of-interest (ROI) from 1<sup>st</sup> row images. The display windows for the reconstructed and difference images are [-160 240] HU and [-90 90] HU.

Figures 2 and 3 demonstrated the representative reconstruction results with case #1, #2 from patients #1 and #2 from different reconstruction networks. It was clearly observed that FBPCONVNet removes most of the artifacts caused by sparse-views, and a few image boundaries and details were further destroyed. HDNet obtained better images but it also led to excessive image smoothing. DDNet improved the details of reconstructed images but the results still contained a few unacceptable artifacts. Unlike the above-mentioned methods, FISTA as one of advanced unrolled deep reconstruction methods had a better performance in sparse-view reconstruction and it can effectively improve the image quality with richer details and clearer edges. However, some tiny features were still lost. In contrast to the counterparts, our MIST-net improved the image quality with the best details and edges.

To display the advantages of the MIST-net, the regions of interests (ROIs) were extracted and magnified in the 3<sup>rd</sup> row of Fig. 2 and Fig. 3. In Fig. 2, we can find that the magnified details marked by the arrows "1" and "2" were badly blurred and destroyed by FBPCONVNet, HDNet and DDNet. One cannot identify the image detail indicated by the arrow "1" from the FBPCONVNet and HDNet. In contrast to FBPCONVNet, HDNet and DDNet, FISTA can achieve a better image. However, it was still inferior to the proposed network. On the other hand, the MIST-net also provided the best image edges. FBPCONVNet, HDNet and DDNet missed details and over-smoothed the edge of tissues in the circle "3". Compared with the three above-mentioned methods, FISTA network almost eliminated artifacts and achieved a not bad image. However, it can be found that the structure of tissue is still slightly fuzzy in the circle "3". The organs in these images could not be clearly highlighted for accurate clinical diagnosis. With the proposed MIST-net, we obtained the best reconstructed result with clear edges and rich details in the image region indicated by the circle "3". To further explain the superiority of our MIST-net in terms of fine texture retention, the easily overlooked details marked with arrows "6", "7" were emphasized in the ROI from case 2. With these regions, it can be inferred that FBPCONVNet, HDNet and DDNet smeared small image features, FISTA provided some features missed by above-mentioned methods but was still limited by the sparse view data, but the finer image features such as arrow "6" were destroyed. The feature indicated by arrow "5" showed that DDNet and FBPCONVNet produced grey intensity shift. The image structure indicated by the circle "4" also demonstrated the advantages of MIST-net in terms of structural fidelity. Observing the images constructed by FBPCONVNet, HDNet, DDNet and FISTA, the feature highlighted by circle "4" was almost lost or damaged. Compared with other methods, MIST-net achieved the best results that look quite similar to the ground truth. More reconstruction experiment results can be found in **Appendix A**.

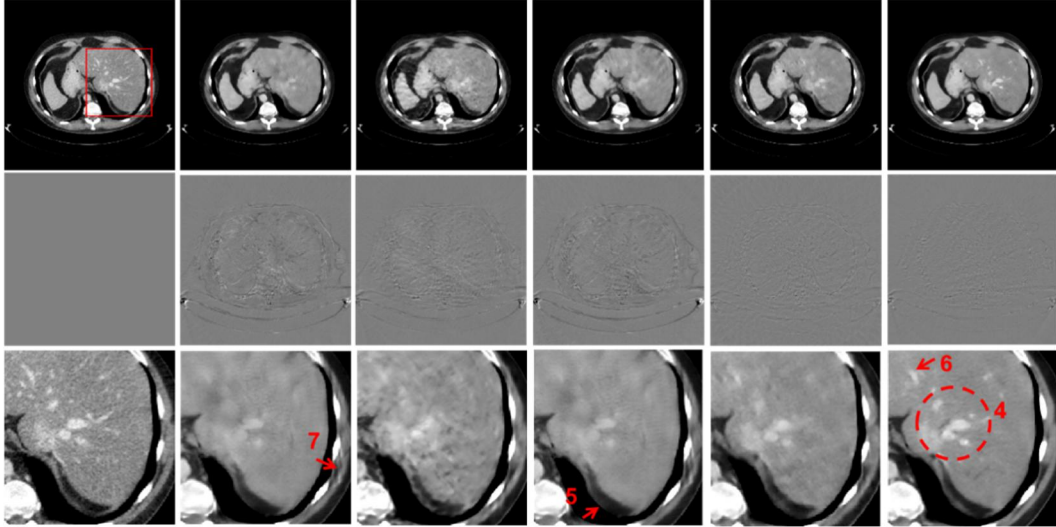


Fig. 3. Visualizations of sparse-view reconstruction in case 2 by using different methods. The 1<sup>st</sup>-6<sup>th</sup> columns represent Ground Truth, FBPconvNet, HDNet, DDNet, FISTA and MIST-net counterparts from 48 views. The 2<sup>nd</sup> row shows the difference images relative to the GT and the 3<sup>rd</sup> row shows the magnification ROIs. The display windows for the reconstructed and difference images are [-160 240] HU and [-90 90] HU.

We also made a quantitative evaluation of all the methods, the results were quantified in Table I. It was observed that our MIST-net network produced the best results than the FBPconvNet, HDNet, DDNet and FISTA methods. Table I demonstrated that FBPconvNet and DDNet achieved the worst performance in PSNR, SSIM, and RMSE, which indicated that the performance of post-processing methods was affected severely by sparse views artifacts. Compared to FBPconvNet only concentrating on image domain, HDNet stacked two U-Net structures respectively in both projection domain and image domain. HDNet had better scores than FBPconvNet, which benefited from the effectiveness of the hybrid domain processing. Meanwhile, FISTA method certainly outperformed FBPconvNet, HDNet and DDNet in all evaluations because of iterative processing. In Table I, our proposed MIST-net method has the smallest RMSEs and the biggest PSNRs and SSIMs in the two cases than those competitors. These quantitative results validated the advantages of the proposed MIST-net demonstrating the best performance. More statistical quantitative results from simulation testing datasets were given in **Appendix A** and they demonstrated our MIST-net can obtain best performance.

TABLE I

QUANTITATIVE EVALUATION OF 48 PROJECTIONS RECONSTRUCTION RESULTS FROM TWO SIMULATED CASES

Views		FBPconvNet	HDNet	DDNet	FISTA	MIST-net	
48	RMSE↓	case1	27.151	24.132	24.603	18.199	<b>16.278</b>
		case2	28.708	22.412	29.111	17.719	<b>15.824</b>
	PSNR↑	case1	38.395	39.419	39.251	41.870	<b>42.839</b>
		case2	37.096	39.246	36.975	41.287	<b>42.269</b>
	SSIM↑	case1	0.9573	0.9625	0.9602	0.9744	<b>0.9800</b>
		case2	0.9647	0.9672	0.9635	0.9752	<b>0.9818</b>

## **B. Clinical Cardiac Validation**

To further verify the performance of MIST-net, the real dataset used in [54] was used. The curved cylindrical detector contains 880 units. There are 2200 views as the full scan. The diameter of field-of-view (FOV) covers  $49.8 \times 49.8 \text{ cm}^2$  with an image matrix of  $512 \times 512$  pixels. The distance from the X-ray source to the system isocenter and the detector array were 53.85 cm and 103.68 cm. Since we have trained the reconstruction network using AAPM datasets, here, we transferred the trained network to evaluate the reconstruction performance using real dataset, which can be benefit to evaluate the generalization ability of our model. We also extracted 48 views from the clinical short scan to test our MIST-net for sparse-view CT imaging. Figure 4 showed the outputs from 48 views using different reconstruction methods. The full-view FBP reconstruction also contained some noise and short-scan artifacts [55]. Compared with these competitors, our proposed MIST-net achieved the best reconstruction results. As shown in the circle "8", MIST-net achieved the structure closest to the ground truth, which adequately embodies the advantages of MIST-net in terms of structural fidelity. Again, MIST-net reconstructed clearer image edges and completer structures. The clearest edges indicated by arrows "10" of our MIST-net results, which cannot be obviously reconstructed by any other networks, strongly confirmed the advantages of proposed MIST-net. In addition, MIST-net was also good at details and feature recovery. The image feature marked by arrow "9" were failed to be recovered by FBPconvNet, HDNet, DDNet and FISTA, however, the proposed MIST recovered this structure. The edges and details in their reconstructed images were hard to be discriminated from two image post-processing methods results, i.e., FBPconvNet and DDNet. For example, the image structure indicated by the arrow "12" cannot be reconstructed by FBPconvNet. Benefited by a dual domain design, HDNet suppressed major artifacts and noise but it still causes fuzziness as well as sparse-view artifacts, which were clearly indicated by the arrows "11" and "13" in Fig. 4. The reconstructed image from FISTA was better than FBPconvNet, HDNet and DDNet. Again, the features indicated by arrows "11" and "12" can be clearly recovered by FISTA. However, in the aspect of edge restoration, FISTA was still worse than our proposed network. For example, the edge marked by arrow "10" cannot be easily recognized by using FISTA network. Furthermore, the detail indicated by the arrow "14" also was destroyed by FISTA-net. The real experiments demonstrated that the proposed network performed consistently better than CNN-based methods in practice. This demonstrated the power of the transformer in the sparse-view CT reconstruction.

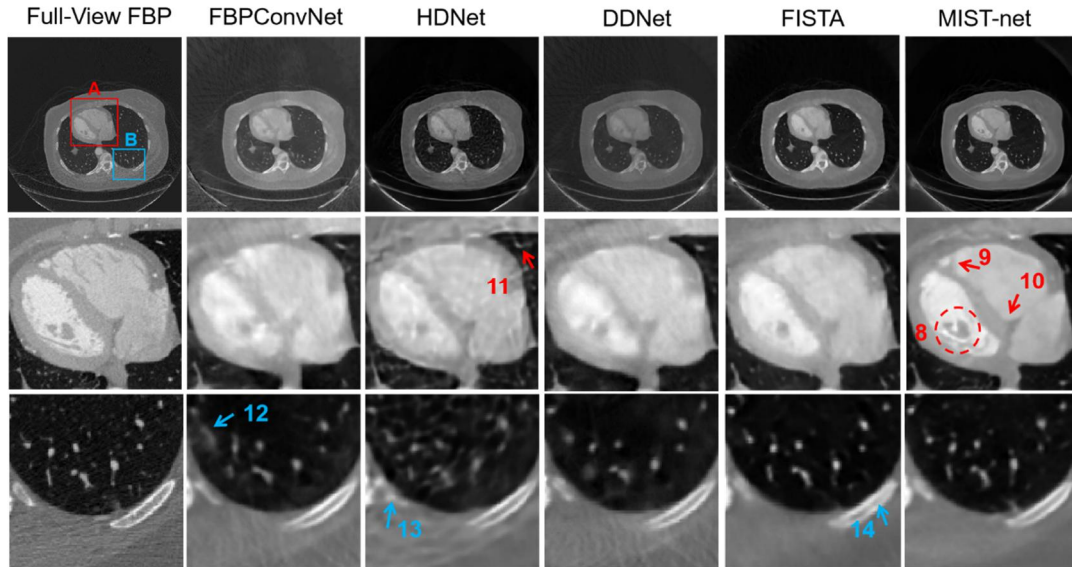


Fig. 4. Clinical cardiac CT reconstructions from sparse-view data by using different networks. The 1<sup>st</sup>-6<sup>th</sup> columns stand for the FBP reconstruction from full-view data, FBPCovNet, HDNet, DDNet, FISTA and MIST-net counterparts from 48 views. The second and third rows show ROIs. The display windows for the reconstructed images are [-800 1000] HU.

#### IV. Ablation Exploration and Generalization Analysis

For analyzing and benchmarking the proposed network MIST-net. Here, we further focused on the ablation explorations to validate the effectiveness of different modules. First, the DU-RecNet represents for the simplified MIST-net which uses two encoder-decoder blocks to replace the edge enhancement reconstruction network and Swin Recformer network. The MU-RecNet denoted the modified DU-RecNet by removing the data consistency module only. All the networks were trained in the same way. As shown in Fig. 5, the residual domain processing indeed is helpful for artifacts reduction and details recovery. Regarding the results indicated by the circle "1" and arrow "2", the DU-RecNet could recover better features than MU-RecNet. Because the residual domain sub-network was designed to eliminate the interpolation errors. The RMSE, PSNR and SSIM indicators results further explained the advantage of the residual domain sub-network.

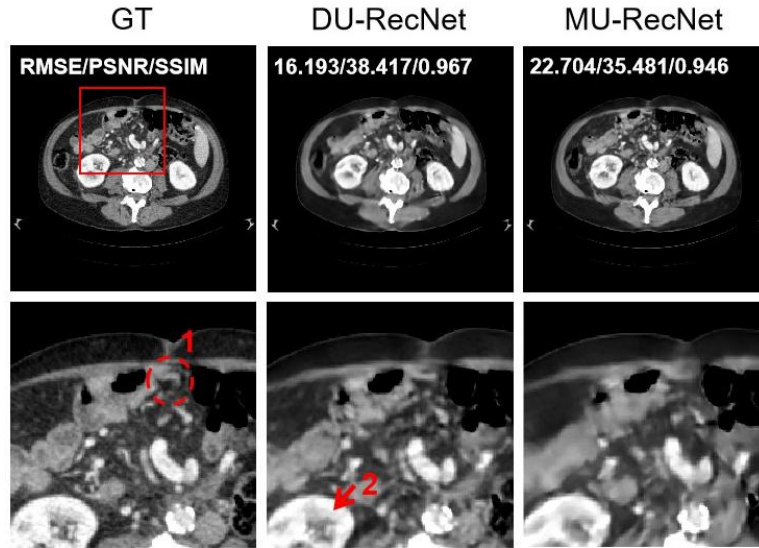


Fig. 5. Reconstruction results in Case 3. The 1<sup>st</sup>-3<sup>rd</sup> columns represent Ground Truth, reconstructions from DU-RecNet and MU-RecNet counterparts from 48 views. The 2<sup>nd</sup> row shows the ROIs. The display window for the reconstructed images is  $[-160\ 240]$  HU.

We also constructed an EE-RecNet to verify the effectiveness of the edge enhancement reconstruction network. Compared to DU-RecNet, EE-RecNet only added the edge enhancement reconstruction network. The architecture of EE-RecNet was similar to MIST-net except that the final Swin Recformer network was replaced by an Unet. Figure 6 showed the reconstruction results from DU-RecNet, EE-RecNet and MIST-net. All the models were trained in the same manner. As shown in the top of Fig. 6 (case #4), the result from DU-RecNet contained a few artifacts due to sparse-view down sampling. The edge enhancement reconstruction module indeed reduces artifacts in image domain and helps to overcome edge over-smoothness. Additionally, we found that the image region marked with the circle "3" was destroyed by DU-RecNet. Both EE-RecNet and MIST-net reconstructed the general outline, but EE-RecNet lost some details such as feature indicated by the arrow "4". Furthermore, from the bottom of Fig. 6 (case #5), one observed that the Swin transformer was also important for high-contrast structural recovery, low-contrast feature reconstruction and textural details preservation. The detail indicated by arrow "5" was blurred by DU-RecNet while MIST-net could reconstruct it well. In addition, the features marked by arrows "6" and "7" were very similar to the ground truth, but they were blurry in the images reconstructed by DU-RecNet and EE-RecNet.

The RMSE, PSNR and SSIM metrics were computed as well to confirm the gain with the edge enhancement reconstruction network. The quantitative results in terms of RMSE, PSNR and SSIM have clearly illustrated the merits of our proposed MIST-net.

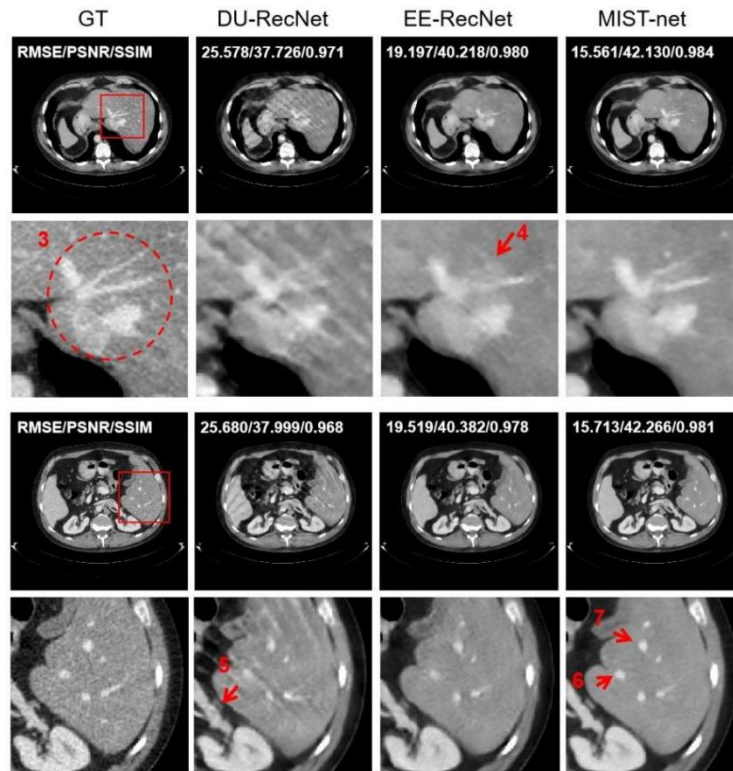


Fig. 6. Comparison of different networks reconstruction results in Case 4 (top) and 5 (bottom). The 1<sup>st</sup>-4<sup>th</sup> columns represent Ground Truth, reconstructions from DU-RecNet, EE-RecNet and MIST-net counterparts from 48 views. The second row of each part shows the ROIs. The display window for the reconstructed images is [-160 240] HU.

To further demonstrate the influence of different modules, we also did an ablation experiment on the real cardiac CT dataset. Figure 7 showed the clinical cardiac reconstructed images from 48 views using relative methods. The performance of MU-RecNet was compromised, and the edges and details were hard to be discriminated. DU-RecNet reconstructed obvious features but still caused hazy edges, which were clearly indicated by the arrow in Fig. 7. EE-RecNet recovered details but produced sparse-view artifacts. Compared with these competitors, the MIST-net delivered the best image quality and evaluation indicators.

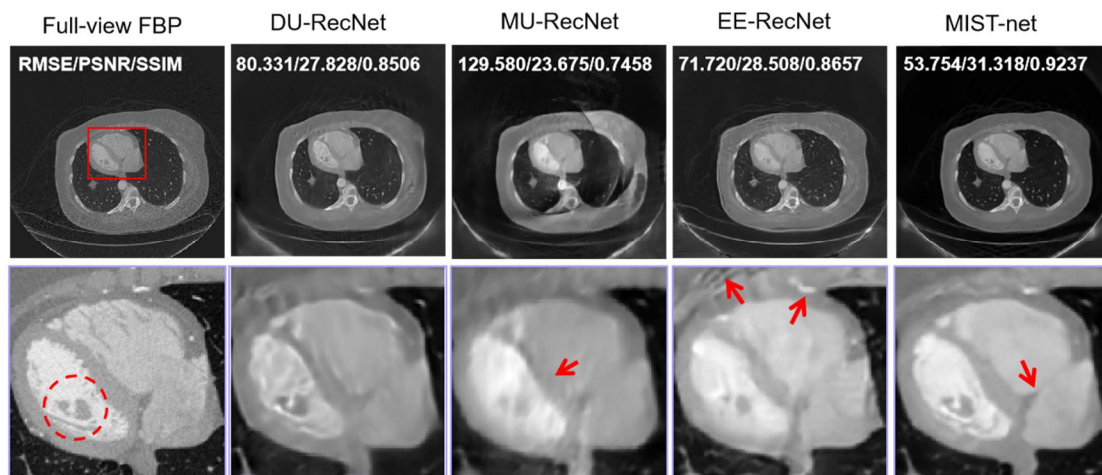


Fig. 7. Comparison of different networks reconstruction results in the real dataset. The 1<sup>st</sup>-5<sup>th</sup> columns stand for the FBP reconstruction from full-view data, DU-RecNet, MU-RecNet, EE-RecNet and MIST-net counterparts from 48 views. The second row shows ROIs. The display windows for the reconstructed images are [-800 1000] HU.

The generalization ability is an important issue for deep learning-based image reconstruction in practice. In this study, the Gaussian noise was added to the images, where the mean and variance are set as 0 and 0.01. Then, the noisy images were employed to verify the ability of reconstruction model against noise attacks during testing process. Figure 8 showed the reconstructed results with different networks. The structures marked with the arrows show that details were blurred by noise using FBPconvNet, HDNet, DDNet, and FISTA. Our proposed MIST-net can obtain better image quality than other competitors. The more detailed noise experiment results were given in **Appendix A**.

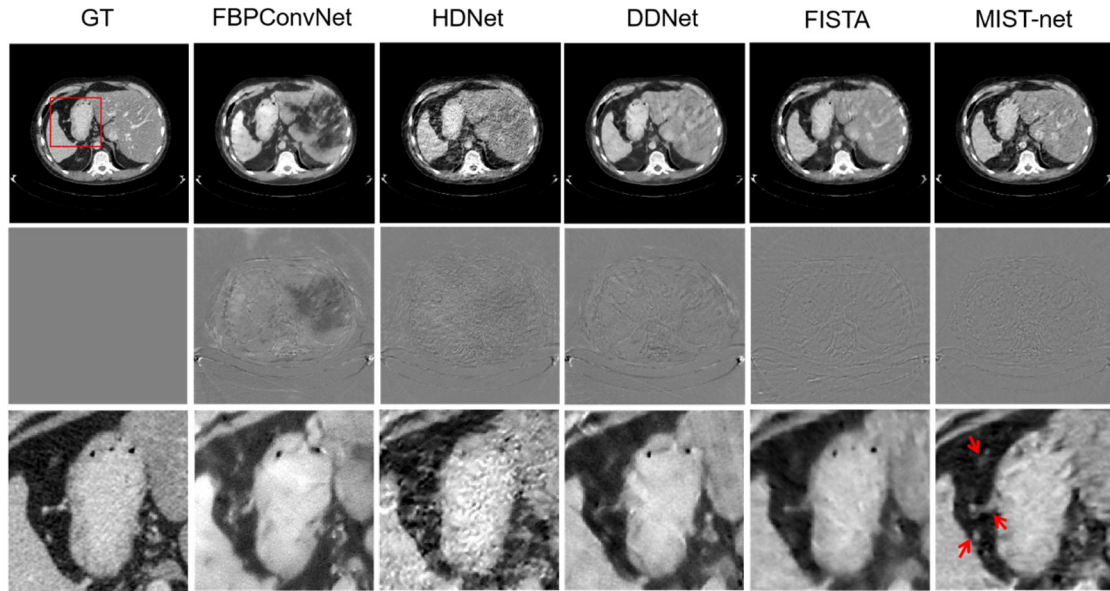


Fig. 8. The generalization of different deep reconstruction networks against noise on simulation datasets. The 1<sup>st</sup>-6<sup>th</sup> columns stand for the ground truth, FBPconvNet, HDNet, DDNet, FISTA and MIST-net counterparts from 48 views. 1<sup>st</sup>-3<sup>rd</sup> rows represent reconstructed results, difference images, and the magnified ROIs.

## V. Discussion and Conclusions

In this paper, we first presented a Multi-domain Integrative Swin Transformer network (MIST-net) for sparse-view CT reconstruction. We designed a multi-domain integrative deep imaging model with sparse-data, where the projection domain and the image domain were respectively responsible for repairing projection data and restoring poor images in the initial recovery stage. Then, the residual projections domain and residual images domain sub-networks were used to eliminate errors and keep the data consistent. To retain image features and enhance image edge, a Sobel filter was introduced in image domain to avoid over-smoothness, which plays an important role to control image quality. More importantly, we proposed Swin Recformer sub-network by combining Swin transformer and convolution to

improve the reconstruction performance. It not only demonstrated the feasibility of transformer-based reconstruction for sparse-view data, but also obtained better image quality than other advanced deep reconstruction networks.

Although the proposed network has demonstrated better performance in ultra-sparse view CT reconstruction, there are still some issues to be addressed. First, the proposed method needed more computational and memory cost than CNN-based methods, which become a challenge of transformer-based application in medical imaging. Second, the transformers had strict requirement on input image size because of positional encoding, which result in the flexibility of transformer-based applications.

We employed our approach to verify sparse-view CT reconstruction on both simulated datasets and clinical dataset, showing that it outperforms CNN-based methods such as FBPconvNet, DDNet, HDNet and FISTA. The experimental results show that the MIST-net were superior to FBPconvNet, DDNet, HDNet and FISTA. Our MIST-net achieved the best results on both simulated datasets and clinical dataset. In summary, this paper presents a multi-domain integrative Swin Transformer reconstruction model. We believe our work will encourage the use of Swin transformer in medical image reconstruction. In the future, we plan to explore the feasibility of our model on related tasks, for example, self-supervised [56], limited-angle CT [43] and low dose CT [57].

## VI. Reference

- [1] M. Bakator, and D. Radosav, "Deep learning and medical diagnosis: A review of literature," *Multimodal Technologies and Interaction*, vol. 2, no. 3, pp. 47, 2018.
- [2] C. Long, H. Xu, Q. Shen, X. Zhang, B. Fan, C. Wang, B. Zeng, Z. Li, X. Li, and H. Li, "Diagnosis of the Coronavirus disease (COVID-19): rRT-PCR or CT?," *European journal of radiology*, vol. 126, pp. 108961, 2020.
- [3] D. J. Brenner, and E. J. Hall, "Computed tomography—an increasing source of radiation exposure," *New England journal of medicine*, vol. 357, no. 22, pp. 2277-2284, 2007.
- [4] J. Bian, J. H. Siewerdsen, X. Han, E. Y. Sidky, J. L. Prince, C. A. Pelizzari, and X. Pan, "Evaluation of sparse-view reconstruction from flat-panel-detector cone-beam CT," *Physics in Medicine & Biology*, vol. 55, no. 22, pp. 6575, 2010.
- [5] J. Bian, J. Wang, X. Han, E. Y. Sidky, L. Shao, and X. Pan, "Optimization-based image reconstruction from sparse-view data in offset-detector CBCT," *Physics in Medicine & Biology*, vol. 58, no. 2, pp. 205, 2012.
- [6] A. Katsevich, "Theoretically exact filtered backprojection-type inversion algorithm for spiral CT," *SIAM Journal on Applied Mathematics*, vol. 62, no. 6, pp. 2012-2026, 2002.
- [7] G. Litjens, T. Kooi, B. E. Bejnordi, A. A. A. Setio, F. Ciompi, M. Ghafoorian, J. A. Van Der Laak, B. Van Ginneken, and C. I. Sánchez, "A survey on deep learning in medical image analysis," *Medical image analysis*, vol. 42, pp. 60-88, 2017.
- [8] C. Niu, J. Zhang, G. Wang, and J. Liang, "Gatcluster: Self-supervised gaussian-attention network for image clustering." pp. 735-751.
- [9] C. Niu, W. Cong, F.-L. Fan, H. Shan, M. Li, J. Liang, and G. Wang, "Low-dimensional manifold constrained disentanglement network for metal artifact reduction," *IEEE Transactions on Radiation and Plasma Medical Sciences*, 2021.
- [10] C. Wang, S. Dong, X. Zhao, G. Papanastasiou, H. Zhang, and G. Yang, "SaliencyGAN: Deep learning semisupervised salient object detection in the fog of IoT," *IEEE Transactions on Industrial Informatics*, vol. 16, no. 4, pp. 2667-2676, 2019.
- [11] H. Chen, Y. Zhang, M. K. Kalra, F. Lin, Y. Chen, P. Liao, J. Zhou, and G. Wang, "Low-dose CT with a residual encoder-decoder convolutional neural network," *IEEE transactions on medical imaging*, vol. 36, no. 12, pp. 2524-2535, 2017.
- [12] Z. Zhang, X. Liang, X. Dong, Y. Xie, and G. Cao, "A Sparse-View CT Reconstruction Method Based on Combination of DenseNet and Deconvolution," *IEEE Trans Med Imaging*, vol. 37, no. 6, pp. 1407-1417, Jun, 2018.
- [13] G. Wang, J. C. Ye, and B. De Man, "Deep learning for tomographic image reconstruction," *Nature Machine Intelligence*, vol. 2, no. 12, pp. 737-748, 2020.
- [14] J. Kyong Hwan, M. T. McCann, E. Froustey, and M. Unser, "Deep Convolutional Neural Network for Inverse Problems in Imaging," *IEEE Trans Image Process*, vol. 26, no. 9, pp. 4509-4522, Sep, 2017.
- [15] M. Bertram, G. Rose, D. Schafer, J. Wiegert, and T. Aach, "Directional interpolation of sparsely sampled cone-beam CT sinogram data." pp. 928-931.
- [16] J. Liu, J. Ma, Y. Zhang, Y. Chen, J. Yang, H. Shu, L. Luo, G. Coatrieux, W. Yang, and Q.

- Feng, "Discriminative feature representation to improve projection data inconsistency for low dose CT imaging," *IEEE transactions on medical imaging*, vol. 36, no. 12, pp. 2499-2509, 2017.
- [17] W. Yu, C. Wang, and M. Huang, "Edge-preserving reconstruction from sparse projections of limited-angle computed tomography using  $\ell_0$ -regularized gradient prior," *Review of Scientific Instruments*, vol. 88, no. 4, pp. 043703, 2017.
- [18] T. Humphries, J. Winn, and A. Faridani, "Superiorized algorithm for reconstruction of CT images from sparse-view and limited-angle polyenergetic data," *Physics in Medicine & Biology*, vol. 62, no. 16, pp. 6762, 2017.
- [19] S. Xie, H. Xu, and H. Li, "Artifact removal using GAN network for limited-angle CT reconstruction." pp. 1-4.
- [20] J. Wang, J. Liang, J. Cheng, Y. Guo, and L. Zeng, "Deep learning based image reconstruction algorithm for limited-angle translational computed tomography," *Plos one*, vol. 15, no. 1, pp. e0226963, 2020.
- [21] D. Hu, J. Liu, T. Lv, Q. Zhao, Y. Zhang, G. Quan, J. Feng, Y. Chen, and L. Luo, "Hybrid-Domain Neural Network Processing for Sparse-View CT Reconstruction," *IEEE Transactions on Radiation and Plasma Medical Sciences*, vol. 5, no. 1, pp. 88-98, 2021.
- [22] Y. Liu, K. Deng, C. Sun, and H. Yang, "A Lightweight Structure Aimed to Utilize Spatial Correlation for Sparse-View CT Reconstruction," *arXiv preprint arXiv:2101.07613*, 2021.
- [23] Q. Zhang, Z. Hu, C. Jiang, H. Zheng, Y. Ge, and D. Liang, "Artifact removal using a hybrid-domain convolutional neural network for limited-angle computed tomography imaging," *Physics in Medicine & Biology*, vol. 65, no. 15, pp. 155010, 2020.
- [24] W. Wu, D. Hu, C. Niu, H. Yu, V. Vardhanabhuti, and G. Wang, "DRONE: Dual-Domain Residual-based Optimization NEtwork for Sparse-View CT Reconstruction," *IEEE Trans Med Imaging*, vol. 40, no. 11, pp. 3002-3014, Nov, 2021.
- [25] A. Zheng, H. Gao, L. Zhang, and Y. Xing, "A dual-domain deep learning-based reconstruction method for fully 3D sparse data helical CT," *Physics in Medicine & Biology*, vol. 65, no. 24, pp. 245030, 2020.
- [26] L. Cheng, S. Ahn, S. G. Ross, H. Qian, and B. De Man, "Accelerated iterative image reconstruction using a deep learning based leapfrogging strategy." pp. 715-720.
- [27] H. Chen, Y. Zhang, Y. Chen, J. Zhang, W. Zhang, H. Sun, Y. Lv, P. Liao, J. Zhou, and G. Wang, "LEARN: Learned experts' assessment-based reconstruction network for sparse-data CT," *IEEE transactions on medical imaging*, vol. 37, no. 6, pp. 1333-1347, 2018.
- [28] Y. Zhang, H. Chen, W. Xia, Y. Chen, B. Liu, Y. Liu, H. Sun, and J. Zhou, "LEARN++: Recurrent Dual-Domain Reconstruction Network for Compressed Sensing CT," *arXiv preprint arXiv:2012.06983*, 2020.
- [29] J. Xiang, Y. Dong, and Y. Yang, "FISTA-Net: Learning A fast iterative shrinkage thresholding network for inverse problems in imaging," *IEEE Transactions on Medical Imaging*, vol. 40, no. 5, pp. 1329-1339, 2021.
- [30] C. Zhang, Y. Li, and G.-H. Chen, "Deep learning enabled prior image constrained compressed sensing (DL-PICCS) reconstruction framework for sparse-view

- reconstruction." p. 1131206.
- [31] A. Vaswani, N. Shazeer, N. Parmar, J. Uszkoreit, L. Jones, A. N. Gomez, Ł. Kaiser, and I. Polosukhin, "Attention is all you need." pp. 5998-6008.
  - [32] A. Radford, K. Narasimhan, T. Salimans, and I. Sutskever, "Improving language understanding by generative pre-training," 2018.
  - [33] A. Radford, J. Wu, R. Child, D. Luan, D. Amodei, and I. Sutskever, "Language models are unsupervised multitask learners," *OpenAI blog*, vol. 1, no. 8, pp. 9, 2019.
  - [34] D. W. Otter, J. R. Medina, and J. K. Kalita, "A survey of the usages of deep learning for natural language processing," *IEEE Transactions on Neural Networks and Learning Systems*, vol. 32, no. 2, pp. 604-624, 2020.
  - [35] A. Dosovitskiy, L. Beyer, A. Kolesnikov, D. Weissenborn, X. Zhai, T. Unterthiner, M. Dehghani, M. Minderer, G. Heigold, and S. Gelly, "An image is worth 16x16 words: Transformers for image recognition at scale," *arXiv preprint arXiv:2010.11929*, 2020.
  - [36] A. Arnab, M. Dehghani, G. Heigold, C. Sun, M. Lučić, and C. Schmid, "Vivit: A video vision transformer," *arXiv preprint arXiv:2103.15691*, 2021.
  - [37] H.-Y. Zhou, J. Guo, Y. Zhang, L. Yu, L. Wang, and Y. Yu, "nnFormer: Interleaved Transformer for Volumetric Segmentation," *arXiv preprint arXiv:2109.03201*, 2021.
  - [38] Z. Liu, Y. Lin, Y. Cao, H. Hu, Y. Wei, Z. Zhang, S. Lin, and B. Guo, "Swin transformer: Hierarchical vision transformer using shifted windows," *arXiv preprint arXiv:2103.14030*, 2021.
  - [39] O. Ronneberger, P. Fischer, and T. Brox, "U-net: Convolutional networks for biomedical image segmentation." pp. 234-241.
  - [40] W. Wu, H. Yu, C. Gong, and F. Liu, "Swinging multi-source industrial CT systems for aperiodic dynamic imaging," *Optics express*, vol. 25, no. 20, pp. 24215-24235, 2017.
  - [41] H. Yu, and G. Wang, "Compressed sensing based interior tomography," *Physics in medicine & biology*, vol. 54, no. 9, pp. 2791, 2009.
  - [42] W. Wu, D. Hu, K. An, S. Wang, and F. Luo, "A high-quality photon-counting CT technique based on weight adaptive total-variation and image-spectral tensor factorization for small animals imaging," *IEEE Transactions on Instrumentation and Measurement*, vol. 70, pp. 1-14, 2020.
  - [43] M. Xu, D. Hu, F. Luo, F. Liu, S. Wang, and W. Wu, "Limited-Angle X-Ray CT Reconstruction Using Image Gradient  $\ell_0$ -Norm With Dictionary Learning," *IEEE Transactions on Radiation and Plasma Medical Sciences*, vol. 5, no. 1, pp. 78-87, 2020.
  - [44] Y. Shen, J. Li, Z. Zhu, W. Cao, and Y. Song, "Image reconstruction algorithm from compressed sensing measurements by dictionary learning," *Neurocomputing*, vol. 151, pp. 1153-1162, 2015.
  - [45] Z. Zha, X. Liu, X. Zhang, Y. Chen, L. Tang, Y. Bai, Q. Wang, and Z. Shang, "Compressed sensing image reconstruction via adaptive sparse nonlocal regularization," *The Visual Computer*, vol. 34, no. 1, pp. 117-137, 2018.
  - [46] J. Dong, J. Fu, and Z. He, "A deep learning reconstruction framework for X-ray computed tomography with incomplete data," *PloS one*, vol. 14, no. 11, pp. e0224426, 2019.
  - [47] I. Sobel, and G. Feldman, "A 3x3 isotropic gradient operator for image processing," a

*talk at the Stanford Artificial Project in*, pp. 271-272, 1968.

- [48] T. Liang, Y. Jin, Y. Li, and T. Wang, "EDCNN: Edge enhancement-based Densely Connected Network with Compound Loss for Low-Dose CT Denoising." pp. 193-198.
- [49] D. Sharifrazi, R. Alizadehsani, M. Roshanzamir, J. H. Joloudari, A. Shoeibi, M. Jafari, S. Hussain, Z. A. Sani, F. Hasanzadeh, and F. Khozimeh, "Fusion of convolution neural network, support vector machine and Sobel filter for accurate detection of COVID-19 patients using X-ray images," *Biomedical Signal Processing and Control*, vol. 68, pp. 102622, 2021.
- [50] J. Chen, Y. Lu, Q. Yu, X. Luo, E. Adeli, Y. Wang, L. Lu, A. L. Yuille, and Y. Zhou, "Transunet: Transformers make strong encoders for medical image segmentation," *arXiv preprint arXiv:2102.04306*, 2021.
- [51] A. Luthra, H. Sulakhe, T. Mittal, A. Iyer, and S. Yadav, "Eformer: Edge Enhancement based Transformer for Medical Image Denoising," *arXiv preprint arXiv:2109.08044*, 2021.
- [52] J. Liang, J. Cao, G. Sun, K. Zhang, L. Van Gool, and R. Timofte, "SwinIR: Image restoration using Swin transformer." pp. 1833-1844.
- [53] C. Bateman, D. Knight, B. Brandwacht, J. Mc Mahon, J. Healy, R. Panta, R. Aamir, K. Rajendran, M. Moghiseh, and M. Ramyar, "MARS-MD: rejection based image domain material decomposition," *Journal of Instrumentation*, vol. 13, no. 05, pp. P05020, 2018.
- [54] H. Yu, G. Wang, J. Hsieh, D. W. Entriakin, S. Ellis, B. Liu, and J. J. J. J. o. c. a. t. Carr, "Compressive sensing-Based interior tomography: Preliminary clinical application," vol. 35, no. 6, pp. 762, 2011.
- [55] G. Zeng, "The fan-beam short-scan FBP algorithm is not exact," *Physics in Medicine & Biology*, vol. 60, no. 8, pp. N131, 2015.
- [56] C. Niu, G. Wang, P. Yan, J. Hahn, Y. Lai, X. Jia, A. Krishna, K. Mueller, A. Badal, and K. Myers, "Noise Entangled GAN For Low-Dose CT Simulation," *arXiv preprint arXiv:2102.09615*, 2021.
- [57] W. Wu, Y. Zhang, Q. Wang, F. Liu, P. Chen, and H. Yu, "Low-dose spectral CT reconstruction using image gradient  $\ell_0$ -norm and tensor dictionary," *Applied Mathematical Modelling*, vol. 63, pp. 538-557, 2018.

## Appendix A

### A.1. More simulated data reconstructions

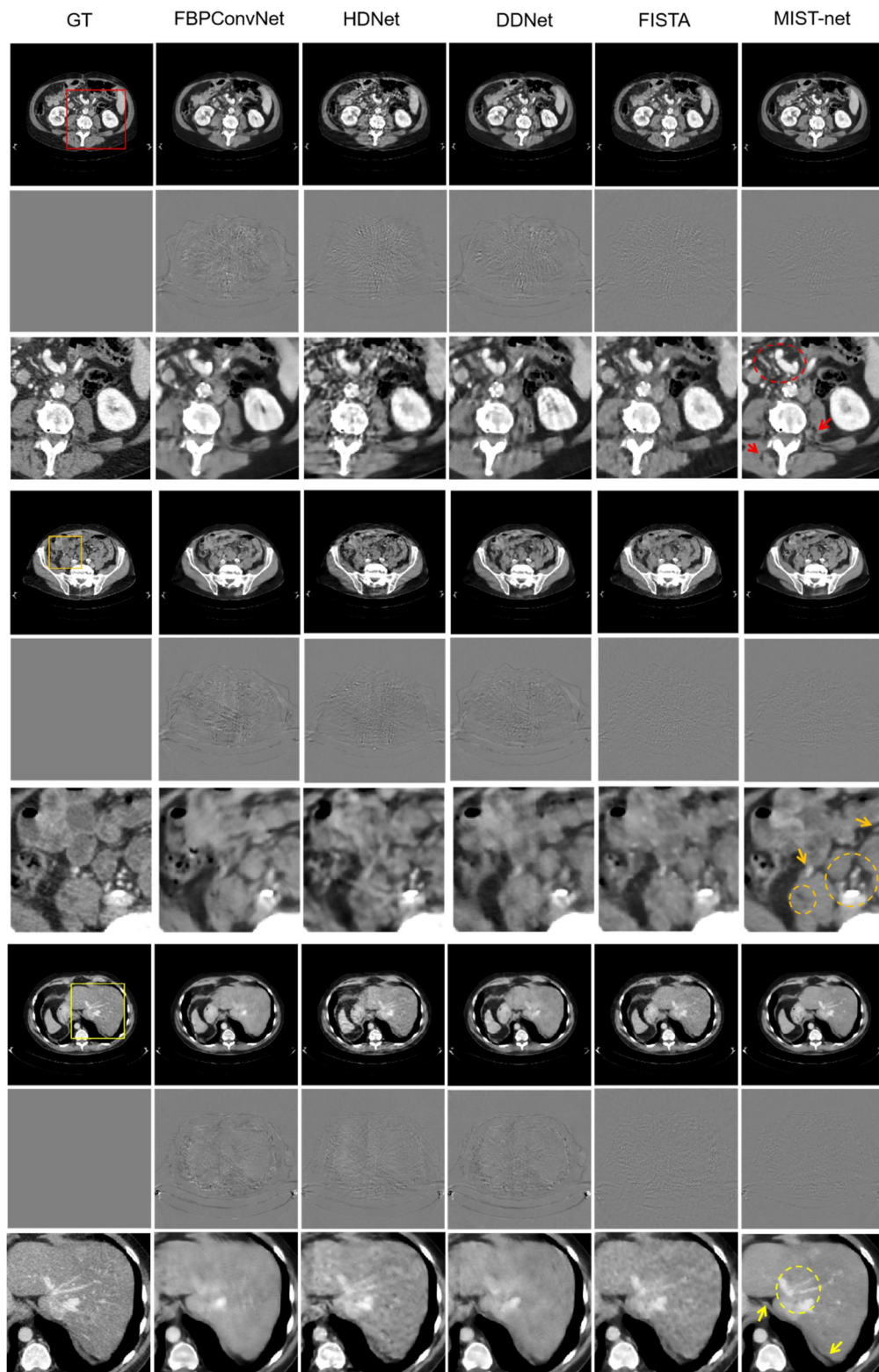


Fig. 9. More simulated data reconstructions from sparse-view data by using different networks. The 1<sup>st</sup>-6<sup>th</sup> columns stand for the FBP reconstruction from full-view data, FBPconvNet, HDNet, DDNet, FISTA and MIST-net counterparts from 48 views. The display windows for the

reconstructed images are [-160 240] HU.

The statistical quantitative evaluations results from testing datasets were computed in terms of RMSE, PSNR and SSIM, and their results were summarized in Table II. It can be seen that our MIST-net can obtain the best quantitative statistical results in terms of mean and standard deviation than other competitors.

TABLE II  
QUANTITATIVE EVALUATION OF 48 PROJECTIONS RECONSTRUCTION RESULTS FROM SIMULATED TESTING DATASETS

Views	Methods	RMSE	PSNR	SSIM
48	FBPconvNet	$27.5520 \pm 3.8158$	$38.0544 \pm 1.4500$	$0.9596 \pm 0.0095$
	HDNet	$23.9574 \pm 3.3687$	$39.2675 \pm 1.2331$	$0.9649 \pm 0.0076$
	DDNet	$25.9597 \pm 3.7597$	$38.5814 \pm 1.6092$	$0.9611 \pm 0.0091$
	FISTA	$19.4109 \pm 2.1991$	$41.0691 \pm 1.0308$	$0.9730 \pm 0.0046$
	MIST-net	<b><math>16.1408 \pm 1.7620</math></b>	<b><math>42.6700 \pm 1.0895</math></b>	<b><math>0.9817 \pm 0.0037</math></b>

### A.2. More noise experiment results

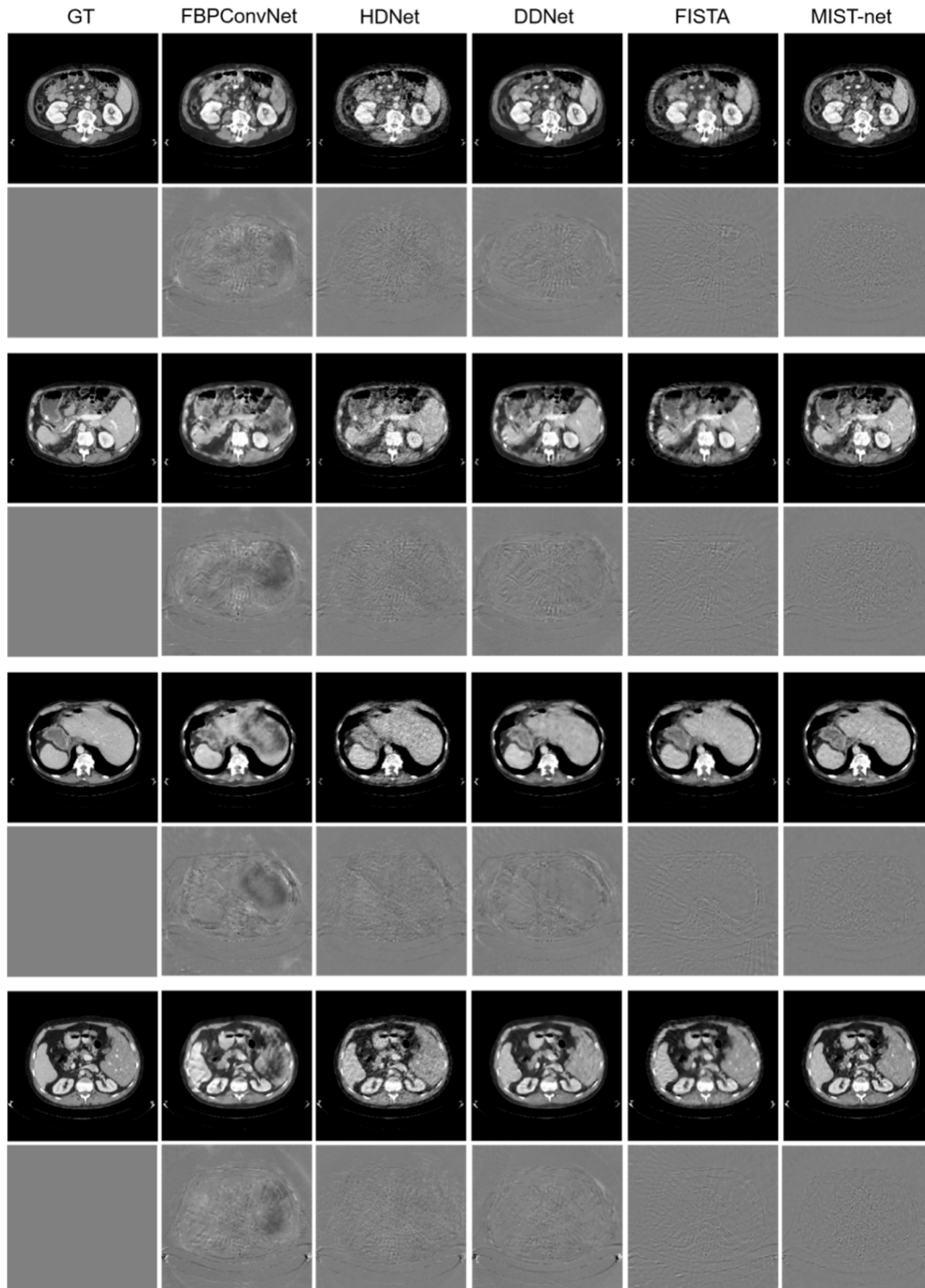


Fig. 10. The generalization of different deep reconstruction networks against noise on simulation datasets.. The 1<sup>st</sup>-6<sup>th</sup> columns stand for the ground truth, FBPconvNet, HDNet, DDNet, FISTA and MIST-net from 48 views. The display window of reconstructed images is [-160 240] HU.